Departure of the thermal escape rate from the Jeans escape rate for atomic hydrogen at Earth, Mars, and Pluto

Jean-Yves Chaufray

Departure of the thermal escape rate from the Jeans escape rate for atomic hydrogen at Earth, Mars, and Pluto

Chaufray J-Y[1]

[1]LATMOS/IPSL, CNRS, UVSQ, Sorbonne-Université, Université Paris-Saclay

Abstract

The recent observations of the Pluto's upper atmosphere by the UV spectrometer Alice on the New Horizons spacecraft mission have shown that it is not in slow hydrodynamic escape as predicted by some fluid models but not by kinetic models. This instrument also detects the Lyman-alpha emission of atomic hydrogen. On Pluto, the hydrogen atoms are produced by the photodissociation of methane and reside in an extended corona around Pluto. Similar to the case at Earth and Mars, the Jeans escape should be the dominant escape process for hydrogen on Pluto due to the low value of the escape parameter at the exobase. However, because of this escape, the velocity distribution at the exobase is truncated at high velocities and the Jeans's escape rate needs to be reduced by a factor B. The goal of this study is to calculate the value of B for the hydrogen on Pluto and check if a plane parallel model, valid to estimate B on Earth and Mars is also valid to calculate B on Pluto.

. We compute B with a plane parallel model for the planets' exospheres, and with a more realistic spherical model to check the validity of the plane parallel model. We find very good agreement between the two models for the current exobase temperatures at Earth, Mars and Pluto. The departure of the thermal hydrogen escape rate from the predicted Jeans escape rate is larger for Mars and Earth than Pluto, even though the escape parameter is lower on Pluto than Mars and Earth. This difference is due to the presence of a minimum in this correction factor for an escape parameter near 3. This minimum is due to the large fraction of particles with a velocity larger than the escape velocity at low escape parameter, leading to an upward-directed velocity distribution

close to the Maxwellian distribution at the exobase. The factor B can be decomposed as the product of two terms: one associated with the departure of the distribution velocity from a Maxwellian distribution at the exobase, and the second, associated with the few collisions above the exobase, reducing the escape rate. The first term has a minimum as a function of exobase temperature, while the second term is a monotonically decreasing function of exobase temperature to an asymptotic value.

1) Introduction

The thermal escape or Jeans escape is an important loss process for hydrogen on Mars, Earth and Pluto. It results from the slow depletion of the tail of the velocity distributions at the exobase, re-populated, partly, by collisions (e.g. Chassefière and Leblanc 2004). The escape rate can be estimated from the Jeans' formula. However, it has long been recognized that thermal escape perturbs the velocity distribution of the escaping species so that Jeans' formula must be corrected to consider the effect of this perturbation (Brinkman 1970). Such corrections have been estimated numerically for the hydrogen on Mars and Earth using plane parallel models (Chamberlain and Campbell 1967, Chamberlain and Smith 1971, Brinkman 1970, Shizgal and Blackmore 1986) and spherical models (Pierrard 2003). The goal of this study is to calculate the correction factor for the hydrogen escape on Pluto and check if a plane parallel model, valid for Earth and Mars is also valid for Pluto. Simulations of Mars and Earth are also performed to validate our model and check the validity of the assumptions used by the previous studies mentioned above.

The effusion velocity can be defined as the escape rate divided by the density at the exobase n_c and the surface area of the exobase S_c (Eq. 11 in Chassefière and Leblanc 2004).

$$U_{eff} = \frac{F_{esc}}{n_c S_c} \quad (1)$$

As discussed later, it is not exactly the upward flow velocity at the exobase because of the few collisions above the exobase.

If the velocity function distribution (vdf) f(V) at the exobase is a Maxwell-Boltzmann distribution at the atmospheric temperature, and if the density and temperature at the exobase are uniform. The escape flux is equal to the Jeans flux which can be computed directly from f(V) at the exobase (Chamberlain 1963)

$$F_{Jeans} = S_c \int_{V>Vesc} f_{MB}(V) V dV \int_{\theta=0}^{\theta=\pi/2} 2\pi \sin\theta \cos\theta \, d\theta \quad (2)$$

Where V is the velocity magnitude, $f_{MB}(V)$ is the Maxwellian-Boltzmann velocity distribution function, θ the angle between the velocity direction and the zenith direction and V_{esc} the escape velocity. The integration provides the usual Jeans formula for the escape flux:

$$F_{Jeans} = S_c \frac{n_c U}{2\sqrt{\pi}} e^{-V_{esc}^2/U^2} (1 + V_{esc}^2/U^2) \quad (3)$$

where U is the thermal velocity: $U = (2kT/m)^{1/2}$ where T is the exospheric temperature, k the Boltzmann's constant, m the mass of the species and n_c its density at the exobase. The effusion velocity is strongly dependent on the escape parameter $\lambda = (V_{esc}^2/U^2)$. However, the loss of the energetic atoms leads to truncated velocity distribution at the exobase which reduces the effusion velocity and therefore the escape flux can differ from the Jeans flux. In that case, the escape flux is more difficult to evaluate and cannot be computed directly from the Maxwell-Boltzmann velocity distribution at the exobase. It may be expressed as

$$F_{esc} = BF_{Jeans} = BS_c \frac{n_c U}{2\sqrt{\pi}} e^{-V_{esc}^2/U^2} (1 + V_{esc}^2/U^2) \quad (4)$$

where *B* is the correction factor due to the truncated vdf (we follow the notation of Fox 2015 for this parameter). Values of B have been estimated numerically for the Earth by several past studies (Brinkmann et al. 1970, Chamberlain and Smith 1971, see also Fahr and Shizgal 1983 and references therein). The estimates of B were done for H and He using Monte Carlo simulations for a plane parallel, isothermal and a monospecies atmosphere (O for Earth and CO_2 for Mars). For H, the values of B by Chamberlain and Smith 1971 and Brinkmann 1970 were in good agreement for the Earth and varying between 0.76 to 0.69 for exospheric temperatures between 1000 and 2000K. For Mars, Chamberlain and Smith 1971 found B between 0.47 to 0.54 for exospheric temperatures between 230 to 730K. They also found a larger correction for the escape of a light species from an atmosphere with a heavy background or in other words, for a given escape parameter λ, B is a decreasing function of the atmospheric average mass m_X.

A new approach was used by Shizgal and Blackmore (1986) to estimate B. They use an iterative matrix method to solve the Boltzmann's equation and derive B for Mars and Earth. Their results were in very good agreement with Chamberlain and Smith (1971) and confirmed that the departure of the distribution from equilibrium is largest for the escape of a light species from an atmosphere with a heavy background gas. For Mars, B was also only computed for temperature between 230 and 730K. Pierrard (2003), used a spectral method to solve the Boltzmann equation, assuming a spherical atmosphere and considering the effect of the gravity on the trajectory of the hydrogen atoms. The author applied this model to study the escape of H and He on Earth and the H escape on Mars for exospheric temperatures at Mars between 230 and 450 K. On Earth, B values were slightly larger than those from Shizgal and Blackmore (1986) and the difference was attributed to different conditions at the lower boundary. On Mars, contrary to Shizgal and Blackmore (1986), a

88 background atmosphere composed of atomic oxygen O near the exobase was considered. A similar
89 value for B was derived, in contradiction with the expected decrease of B with m_X.

90 At Mars, the global thermospheric simulations and the recent MAVEN observations suggest a
91 dayside exospheric temperature between 150 – 400K and a nightside exospheric temperature near
92 130K (Gonzalez-Galindo et al. 2015, Bougher et al. 2017). Moreover, near the exobase, the Martian
93 atmosphere is not a purely CO_2 atmosphere but atomic oxygen can become an important species
94 (Bougher et al. 2015). On Pluto, the recent observations of the upper atmosphere by Alice/New
95 Horizons have shown that the atmosphere is not in slow hydrodynamics escape as predicted by
96 some models (Gladstone et al. 2017). This instrument also detects the Lyman-alpha emissions of
97 atomic hydrogens, produced by the photodissociation of methane (Gladstone et al. 2019).
98 Therefore, an estimate of B for Pluto's conditions is needed since the escape parameter is low and
99 the velocity distribution function at the exobase could be strongly modified by the escape.
100 Moreover, the validity of the plane parallel should be checked with a more physical model in the
101 B calculation. In this paper, we perform several Monte Carlo simulations to estimate B. After
102 presenting the model (section 2), we apply it to Earth (section 3), Mars (section 4), Pluto (section
103 5) and conclude in section 6.

104 **2) Model**

105 The model used to estimate B of the atomic hydrogen thermal escape rate is a Monte Carlo model.
106 In this model, several hydrogen test particles are launched from the lower boundary z_{low} in an
107 isothermal or non-isothermal thermosphere and followed until they escape or return to z_{low}. In this
108 study, we used two versions of the models:

109 The first version is a very simple model, similar to the model used by Chamberlain and Smith
110 (1971) and Shizgal and Blackmore (1986): It is a plane parallel atmosphere with a uniform density

and temperature (slab atmosphere). The effect of the gravity on the test particles trajectory is neglected except at the upper boundary where the test particles are specularly reflected if their velocity is lower than the escape velocity. The thickness Δ of the layer between the lower and the upper boundaries is of 10 mean free paths subdivided into 50 equal layers. The atmosphere is composed of only one species O (Earth), CO_2 (Mars), or N_2 (Pluto). This model is very fast but only valid to estimate B.

The second version is a more realistic model, closer to Pierrard (2003), considering a spherically symmetric multi-species atmosphere, with a background atmosphere in hydrostatic equilibrium. The temperature can be uniform or non-uniform. The effect of the gravity on the trajectories of the test particles is included and the upper boundary is at an altitude well above the expected exobase, where collisions are negligible. The velocity distribution of the test particles injected in the simulation at the lower boundary is a Maxwellian-Botzmann Flux (MBF) distribution (Brinkmann et al. 1970). When a test particle reaches the upper boundary with a velocity lower than the escape velocity, the final location and the time of flight of the particle returning to the domain is calculated analytically (Butler 1997). Other effects like radiation pressure, gravitational effects of moons (e.g. Beth et al. 2014, Baliukhin et al. 2019) are not considered in this study. For the more realistic spherical simulations, the loss of hydrogen atoms by photoionization have been included using an average loss time $\tau = \tau_0 d^2$, where $\tau_0 = 1.4 \times 10^7$ s is the ionization lifetime at 1 AU (Huebner 1992), and d the sun-planet distance in AU. However, for all our simulations, the ionization has only a minor effect on B and may be neglected. The effect of Charon on the hydrogen escape is most likely negligible as for N_2 and CH_4 (Tucker et al. 2015, Hoey et al. 2017).

The spherical model is slower than the plane parallel model but is used not only to estimate B but also other macroscopic parameters (hydrogen density, kinetic temperature) in planetary upper atmosphere

For each simulation, several millions of test particles are used. All test particles have the same weight *W* (i.e. the number of real particles represented by one test particle) chosen at an arbitrary value, that should depend on the net hydrogen flux at the lower boundary. Therefore, all the simulated density profiles will be normalized because the absolute value is proportional to the arbitrary weight of the test particles. The computed velocity and kinetic temperature are independent on the weight and will be presented in physical units.

To estimate the number of collisions with the background atmosphere for each test particles during the time step *dt*, we use the no-time-counter scheme used by Bird (1994) as done in the LATMOS Exospheric Global Model (EGM) (Leblanc et al. 2017): A maximal number of collisions is first estimated using a majorant $(\sigma V_r)_{max}$ of the product $\sigma(V_r)$ x V_r, where $\sigma(V_r)$ is the collision cross section and V_r the relative velocity of the test particle and the atmospheric particle. This maximal number of collisions N_{max} is given by

$$N_{max} = [n(X) + n(Y) + \ldots](\sigma V_r)_{max} \; dt \quad (5)$$

Where n(X); n(Y) are the density of species X and Y at the altitude of the test particle.

Then, for each collision, the atmospheric species (X, Y, ...) with which the test particle collides is chosen using the local relative abundance of the species. The velocity vector of the atmospheric particle is derived randomly using a Maxwellian distribution at the local temperature, and the relative velocity vector is calculated to compute the product $\sigma(v_r)v_r$. A second test is then performed:

$$\frac{\sigma(V)V_r}{(\sigma V_r)_{max}} > r \quad (6)$$

where, r is a random number uniformly distributed between 0 and 1. If this test is fulfilled, the collision is accepted, while if it is not fulfilled the collision is rejected. For most of the simulations, we used a hard sphere model to describe the collisions ($\sigma(V_r) = \sigma_0$). Because N_{max} is never an integer, we always consider $N_{max} + 1$ collisions and the last collision is treated with the algorithm presented above only if the following condition is fulfilled: $[N_{max} - E(N_{max})] > r$, where $E(N_{max})$ is the integer part of N_{max}. For example, if $N_{max} = 19.50$, the maximal number of collisions will be 20, but the last collision will have a probability of 50% to be discarded before using the rejection algorithm presented above. This method differs from the method used by Brinkman (1970). The method used by Brinkman (1970) was based on the inversion of the distribution function of the relative velocity, knowing the hydrogen velocity. This inversion was performed from pre-computed table of the discretization of the cumulative distribution function of the relative velocity for different values of the hydrogen velocity. This method is fastidious because the precomputed tables depend on the cross section (or interaction potential). The method of Bird (1994) can be used systematically for any cross sections, without any precomputation tables. Its only drawback is that it is less optimal because if $(\sigma V)_{max}$ is too large, a large number of possible collisions will finally be rejected. But this drawback is not very important given the increasing possibility of computers now compared to the years 1970s. To validate our scheme, we compared the simulated collision frequency ν at low altitudes z, (where the fdv are not perturbed) to the theoretical value: $\nu(z) = n_a(z)\sigma\langle V_r\rangle$ (Chapman and Cowling 1970) where n_a is the atmospheric density ("background" density), σ the collision cross section (equal to 3×10^{-15} cm^2) , $\langle V_r\rangle$ is the average relative velocity, given for Maxwellian distributions by $\langle V_r\rangle = (8kT/\pi\mu)^{1/2}$, and μ is the reduced mass and find a very good agreement.

B is computed following Chamberlain and Smith (1971): The simulated escape rate $F_{e,sim}$ is proportional to the number of escaping test particles N_{esc} :

$$F_{e,sim} = WN_{esc} \quad (7)$$

The weight W is related to the arbitrary flux chosen at the lower boundary F_0 by:

$$F_0 = WN_{test} \quad (8)$$

For a Maxwellian-Boltzmann Flux distribution, this flux is also related to the arbitrary density n_0 at the lower boundary and the average velocity $\langle V_0 \rangle = 2U_0/\pi^{1/2}$ by

$$F_0 = \frac{n_0 U_0}{2\sqrt{\pi}} S_0 \quad (9)$$

where $S_0 = 4\pi R_0^2$ for the spherical model and is arbitrary for the plane parallel model. Then, the escape flux can be expressed as

$$F_{e,sim} = \frac{n_0 U_0}{2\sqrt{\pi}} S_0 \frac{N_{esc}}{N_{test}} \quad (10)$$

B is the ratio between the simulated escape flux and the Jeans escape flux at the exobase (Eq. 4) and therefore, B can be numerically estimated by

$$B = \frac{n_0}{n_c} \frac{N_{esc}}{N_{test}} \frac{S_0}{S_c} \frac{e^{\lambda_c}}{(1+\lambda_c)} \frac{U_0}{U} \quad (11)$$

For the plane parallel simulations $S_0/S_c=1$ and for the spherical simulations $S_0/S_c=(R_0/R_c)^2$. If the atmosphere is isothermal $U_0/U=1$.

For the plane parallel model, the exobase is at one mean free path below the upper boundary, while for the spherical model, the exobase altitude can equivalently be derived from the equality between the atmospheric scale height and the mean free path. For the plane parallel model, because we neglect the vertical variations of λ, $N=N_{test}(1+\lambda_c)e^{-\lambda_c}$ is the number of test particles with an initial

velocity larger than the escape velocity. It would be proportional to the escape flux if the collisions were neglected. If we note $F_{e,0}$ the flux of particle with a velocity larger than the escape velocity at the lower boundary, $F_{e,0} = Wx\ N_{test}(1+\lambda_c)e^{-\lambda c}$. Replacing, N_{esc} by $F_{e,sim}/W$ (Eq. 7), and using $S_c/S_0 = 1$ and $U = U_0$ for the plane parallel isothermal model, it leads to $B = (n_0/n_c) \times (F_{e,sim}/F_{e,0})$ which is Eq. 11 in Chamberlain and Campbell (1967). The few collisions above the exobase do not change the escape rate when the velocity distribution function at the exobase is a Maxwellian distribution because every collision from particle *a* to *b* is balanced by a collision from particle *b* to *a* due to the detailed balancing properties of the Maxwellian distribution (Chamberlain 1963). However, when the velocity distribution function departs from the Maxwellian distribution, this balancing property is not valid anymore, and the few collisions above the exobase will change the escape rate. In other words, when the velocity distribution function is not Maxwellian, B can be written as the product of two terms B = A x G. A is the ratio between the "effusion velocity" computed from the distribution at the exobase U_{eff}^*

$$U_{eff}^* = \frac{1}{n_c}\int_{V>Vesc} f(V)VdV \int_{\theta=0}^{\theta=\pi/2} 2\pi \sin\theta \cos\theta \, d\theta \qquad (12)$$

and the Jeans effusion velocity $U_{Jeans} = F_{Jeans}/n_c S_c$. G is the ratio between the real effusion velocity U_{eff} (defined by Eq. 1) and U_{eff}^*. In general, U_{eff} and U_{eff}^* are not equal (except for a Maxwellian distribution), due to the few collisions above the exobase.

$$B = \frac{U_{eff}}{U_{Jeans}} = \frac{U_{eff}}{U_{eff}^*}\frac{U_{eff}^*}{U_{Jeans}} = G \times A \qquad (13)$$

3) Earth simulations

3.1) Variations of B vs. Exospheric temperature

B values for atomic hydrogen, derived from the first model (plane parallel) and the second model (spherical model with a hydrostatic atmosphere of atomic oxygen) simulated for different exospheric temperatures are displayed on Fig. 1.

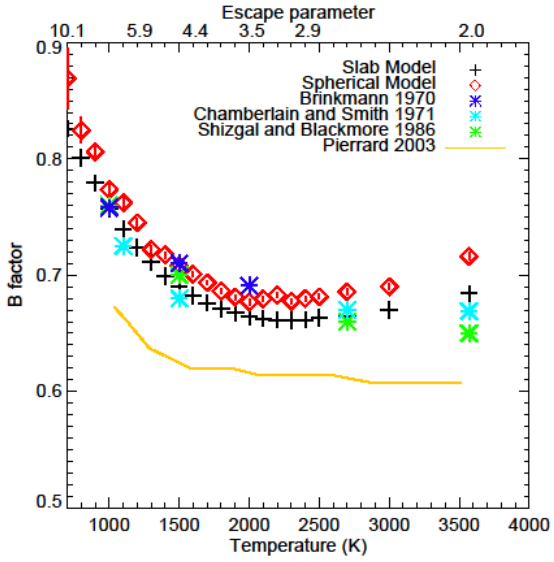

Fig. 1: Simulated B factor for the Earth for the slab isothermal model (black) and the spherical isothermal model (red) at different atmospheric temperatures for Earth. The results from other studies (slab models): Chamberlain and Smith (1971) and Shizgal and Blackmore (1986); spherical (Pierrard 2003) are also displayed for comparisons. The error bars from the Monte Carlo simulations have been added for the spherical model (vertical red lines).

For the first model, we use 10^8 test particles, while only $5x10^6$ test particles were used for the spherical model to reduce the simulation time. For the spherical model, A, B and G values are computed from output obtained every 100,000 test particles (so 50 values are computed since, 5,000,000 test particles are simulated). Because the test particles are independent, the different values of B are also independent. The mean value and the uncertainty on the mean deduced from the 50 values, are shown in Fig. 1. For most of the simulations, the error bars are lower than the symbol size, except in case of large values of the escape parameter, where a very small fraction of test particles escapes.

The range of escape parameters λ (for atomic hydrogen) for the slab model is between 1.98 (T = 3570K) and 10.1 (T = 700K). For the second model, the lower boundary is chosen at 240 km and the upper boundary at 2000 km, well above the exobase (at ~500 km, depending on the atmospheric temperature), and the spatial resolution is uniform equal to 12.5 km. The O density at z_{low} = 240 km is fixed at 1.2×10^9 cm^{-3} for any temperatures (Dickinson et al. 1984), and decrease exponentially with the altitude with a scale height $H_a = kT/m_O g(r)$, where *g(r)* is the gravitational acceleration at *r*, *k* the Boltzmann's constant, m_O the atomic oxygen mass and *T* the temperature.

The agreement between the two models is within 3% for the current temperatures at the exobase (between 700K and 2000K) which confirms that the following assumptions (plane parallel geometry, neglecting the gravity, assuming a uniform atmosphere) are good assumptions to estimate B. The agreement between the two models is not a surprise, since the thickness Δ (~ 30 km) of the collisional region near the exobase impacting the effusion velocity is much smaller than the Earth radius (Brinkmann et al. 1970).

Here, we also confirm that the effect of the gravity on the test particles trajectory can be neglected. The Knudsen number Kn is defined by $Kn(z)=(N_a(z)\sigma)^{-1}$ where $N_a(z)$ is the atmospheric column density above the altitude z. At the exobase Kn = 1 by assumption (see section 2). If we assume that at z_l, defined by $Kn(z_l) = 0.1$, the velocity distribution is not affected by the escaping particles and is well described by a Maxwellian distribution, then the altitude of the lower boundary z_{low} should be at z_l or below. Assuming a barotropic distribution of the atmospheric density and an isothermal atmosphere:

$$n_a(z) = n_a(z_{exo})e^{-(z-z_{exo})/H} \quad (14)$$

The column density between z_l and the exobase altitude z_{exo} is

256 $$N_a(z_l) - N_a(z_{exo}) = n_a(z_{exo}) H_a \left(e^{(z_{exo}-z_l)/H_a} - 1\right) \quad (15)$$

257 Because, $\sigma n_a(z_{exo}) H_a = 1/Kn(z_{exo}) = 1$, the altitude z_l is given by

258 $$z_l = z_{exo} - H_a \, ln(10) \approx z_{exo} - 2.3 H_a \quad (16)$$

259 For the typical exospheric temperature on Earth (T between 1000 – 2000 K), H_a varies from 50 to
260 100 km and the exobase altitude z_{exo} is ~ 500 km. Therefore, $2.3H_a$ ~ 115 to 230 km and z_l = 270
261 – 375 km, depending on the exospheric temperature. In all the simulations presented in this section,
262 the altitude of the lower boundary z_{low} is 240 km, below z_l. In this altitude range, the thermospheric
263 temperature is almost constant (Dickinson et al. 1984), and therefore the assumption of an
264 isothermal layer is a good assumption.

265 Our results are also in agreement with the results from Chamberlain and Smith (1971), Shizgal and
266 Blackmore (1986) but differ systematically by 10% from Pierrard (2003). This difference is not
267 understood and could be due to numerical effects in the Pierrard model. The small difference ~3%
268 for T =3570K with Chamberlain and Smith (1971) that may be due to numerical uncertainties in
269 those previous models. The simulated uncertainties on B from the spherical simulations are also
270 displayed in Fig. 1 and are generally lower than the symbol size and therefore can't explain the
271 difference. Varying the elastic cross section from 10^{-15} cm^2 to 10^{-14} cm^2 does not change the B
272 values (within the magnitude of the numerical noise ~ 1%).

273 We can also notice a minimum of B between 2000 - 2500 K (λ ~ 3). When λ becomes very small,
274 most of the particles have a velocity larger than the escape velocity and then a large fraction of test
275 particles is allowed to escape. The velocity distribution function at the exobase is therefore close
276 to a Maxwellian distribution. This point is studied in more details in section 5. As shown in Eq. 13,
277 B can be decomposed into two terms A and G describing the relative effect of the non-Maxwellian

278 distribution at the exobase and the effects of the few collisions above the exobase. These two factors
279 are displayed on Fig. 2, we can see, as demonstrated by Chamberlain (1963), that *G* is close to 1
280 and then $A \sim B$ at low temperatures.

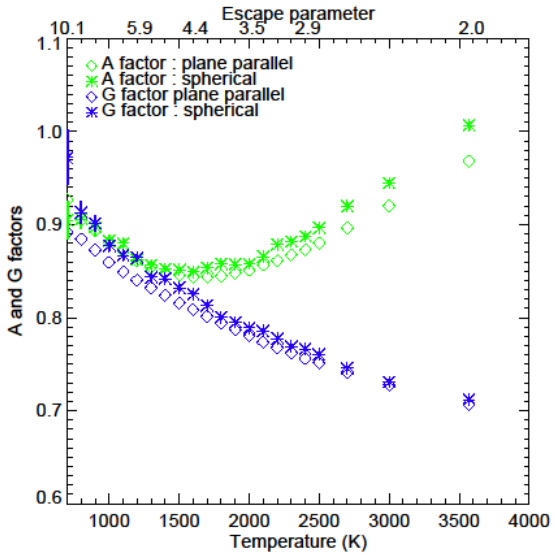

281

282 *Fig. 2: Simulated A and G factor for the Earth for the slab isothermal model (diamonds) and the spherical isothermal*
283 *model (stars) at different atmospheric temperatures for Earth.*

284 *A* reaches a minimum between T = 1500 and 2000 K, and then increase for T > 2000 K while *G*
285 always decreases with the temperature. While the estimates of A and G are slightly noisy due to
286 the limited number of escaping test particles, particularly at large escape parameters, the trends for
287 the plane parallel and spherical model are very similar for the two factors. The major cause on the
288 departure from the Jeans escape flux is due to *G*, which means that the effusion velocity computed
289 by integration of the velocity distribution function at the exobase (Eq. 11) is close to the Jeans
290 effusion velocity at the atmospheric temperature, but the few collisions occurring above the
291 exobase modify the escape rate. For the plane parallel case, in order to derive the asymptotic values
292 of B, A and G, we also perform one simulation with $\lambda = 0$ (Vesc = 0). In that case the escape is

independent on the velocity, since all the test particles reaching the upper boundary will escape whatever their velocity. The asymptotic values are B = 0.84, A = 1.43 and G = 0.59, which confirms that B is still increasing for T > 3570 K. The downward directed distribution at the exobase is much more depleted than the upward directed distribution and leads to $1 < A < 2$ (see appendix). While the velocity distribution of the upward directed particles has a Maxwellian shape, the full distribution is not Maxwellian, due to the large depletion of downward directed particles. This Non-Maxwellian velocity distribution does not possess the properties of detailed balancing. If the collisions above the exobase were fully neglected, $U_{eff} = U_{eff}^*$ (all particles leaving the exobase with V > Vesc will really escape). Moreover, the velocity distribution would be strongly asymmetric with a lack of downward directed particles at $V > U_{eff}$ compared to the upward directed particles. The collisions above the exobase are not negligible. Their net effect is to reduce the asymmetry of the velocity distribution. Because the number of upward directed particles is larger than the number of downward directed particles, more upward directed particles are converted to downward directed particles by collisions than the inverse. Then Ueff < Ueff* (G < 1). Obviously, this limit case is not realistic since for $\lambda = 0$, the exobase should be very far and the plane parallel assumption is not valid anymore. Since B depends on the few collisions occurring above the exobase, B should be sensitive to the details of the differential cross section.

3.2) Sensitivity to the cross section

To check the sensitivity to the collisional cross section, we performed simulations with the hard sphere cross sections and with an angular-dependent forward peaked cross section taken from Lewkow et al. (2014), for an exospheric temperature T = 3000K using the spherical model only. In the studied energy range, the total cross section σ_{tot} for O-H collisions from Lewkow et al. (2014)

315 is equal to $3.3x10^{-15}$ cm^2 and is independent on the energy, while the differential cross section
316 follows an analytical law

317 $$\frac{d\sigma}{d\theta}(\theta) = \frac{\sigma_{tot}}{2\pi ln\left(\frac{\theta_{max}}{\theta_{min}}\right)} \frac{1}{\theta sin\theta} \quad (17)$$

318 with θ_{max} and θ_{min}, the maximal and minimal values of the scattered angle (0.01° and 170°
319 respectively). These properties are adapted to check the sensitivity of B on an angular-dependent
320 forward peaked cross section.

321 The B, A and G parameters for simulations assuming an isotropic and forward-peaked cross
322 sections, for the same total cross section ($3.3x10^{15}$ cm^2) are respectively: 0.67, 0.94 and 0.71 for
323 the isotropic differential cross section and 0.75, 0.79, 0.95 for the forward-peaked differential cross
324 section. As expected, B and G are larger for the simulations with the forward-peaked cross section.
325 When the cross section is forward-peaked, most of the atoms crossing the exobase from below with
326 a velocity larger than the escape velocity will not be deviated by collisions and will escape so the
327 value of G is larger than the value computed with an isotropic differential cross section where the
328 deviations produced by collisions are more important. On the other side, because less particles with
329 a velocity larger than the escape velocity are coming back to the exobase, the tail of the velocity
330 distribution at the exobase is more depleted and the A factor is reduced. The global effect is a slight
331 increase of B.

332 **4) Mars Simulations**

333

334 **4.1) Variations of B vs. Exospheric temperature**

335 On Mars, the atmosphere below the exobase is mostly composed of CO_2 (e.g. Bougher et al. 2015).
336 We apply the same simple plane parallel model to Mars in order to derive B for H in a purely CO_2

atmosphere. The assumptions correspond to the assumptions used by Chamberlain and Smith (1971) and Shizgal and Blackmore (1986) to study B for atomic hydrogen on Mars. Contrary to Shizgal and Blackmore (1986), we compute it for a more realistic range of exospheric temperature at Mars from 130K (expected temperature near the nightside) to 400K (temperature expected at the dayside near solar maximum conditions). For all the spherical simulations, we use a CO_2 density of 10^{10} cm^{-3} at 140 km, and an exponential decrease with altitude. The altitude range is 140 to 640 km with a spatial resolution of 6.25 km.

B vs. the exospheric temperature is displayed in Fig. 3.

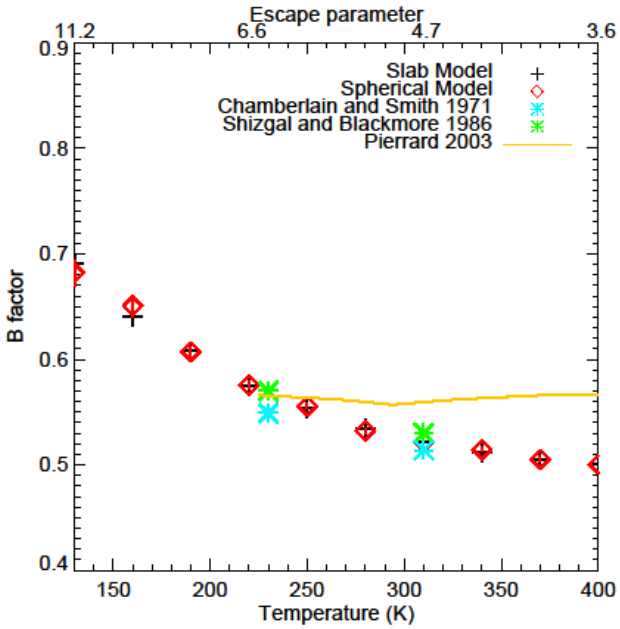

Fig. 3: Simulated B factor for Mars for the slab isothermal model (black) and the spherical isothermal model (red) at different atmospheric temperatures. The results from other studies (slab models): Chamberlain and Smith (1971) and Shizgal and Blackmore (1986); spherical (Pierrard 2003) are also displayed for comparisons.

The range of escape parameters λ for the slab model is 3.6 (T = 400K) and 11.1 (T = 130K). Our results are in very good agreement with the results of Shizgal and Blackmore (1986) and Chamberlain and Smith (1971) at the temperatures simulated by these authors. B values derived

353 from both models are very close (Fig. 3). This result confirms that B can be accurately estimated
354 with the very simple assumptions used in the plane parallel code. The simulated B values are
355 slightly lower than the B values computed by Pierrard (2003). As found by Chamberlain and Smith
356 (1971), for a given λ value, B is lower on Mars than for Earth because of the heavier species (CO_2
357 vs O) involved in the collisions and therefore, B values computed by Pierrard 2003 are partly larger
358 because a purely oxygen atmosphere was considered. The chosen range of exospheric temperature
359 leads to escape parameters $\lambda > 3$ for all the cases, and therefore the minimum of B near $\lambda \sim 3$ is not
360 reached in these simulations. An increase of B can be noted in the simulations of Chamberlain and
361 Smith (1971) at lower λ ($T > 700K$) but was not discussed. However, it is not proved that such
362 exospheric temperatures could have occurred on Mars, even in the past (Terada et al. 2016).

363 The decomposition of B into A and G is displayed on Fig. 4. The trends for the plane parallel and
364 the spherical models are in good agreement, although the values are noisy for the spherical
365 simulations due to a lower number of simulated escaping test particles, especially at low
366 temperatures. Both parameters decrease with the temperature.

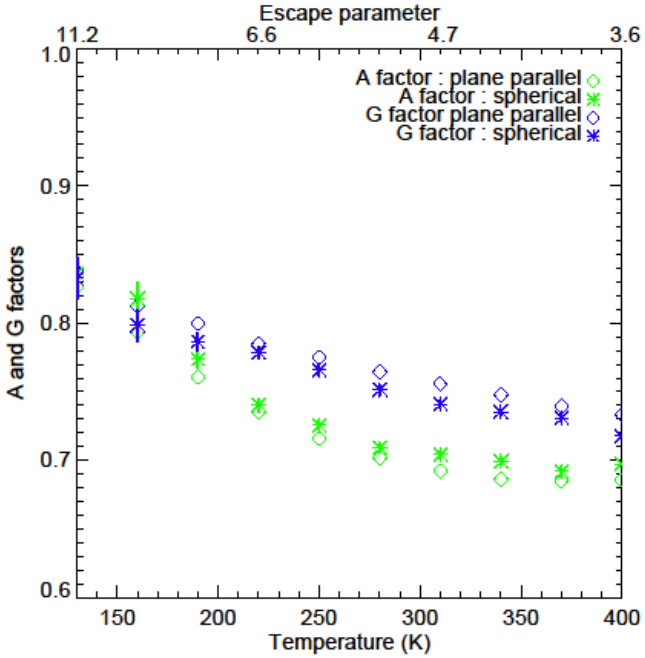

Fig. 4: Simulated A and G factor for Mars for the slab isothermal model (diamonds) and the spherical isothermal model (stars) at different atmospheric temperatures.

4.2) Effect of the composition of the atmosphere

Since past studies have used different species as the main atmospheric species near the exobase: CO_2 (e.g. Shizgal and Blackmore 1986) and O (Pierrard 2003), we also test the effect of the main species on B, using the spherical model only. B values obtained for a purely atomic oxygen atmosphere are close to those obtained for the Earth for similar λ values and differ significantly from the values simulated by Pierrard (2003). We also perform a simulation with both species, using a relative volume mixing ratio $nO/nCO_2 = 0.01$ at 140 km (Krasnopolsky 2002), in all these simulations, we assume a constant collisional cross section and the same cross section for hydrogen collisions with O and CO_2. For this multi-component atmosphere, the exobase altitude is derived from the equality between the total density scale height and the mean free path defined by $(n_O\sigma_O+n_{CO2}\sigma_{CO2})^{-1}$ where σ_O (σ_{CO2}) is the collision cross section between H and O (CO_2).

The results obtained for the three sets of assumptions are displayed on Fig. 5. As expected, for the two-species atmosphere B values are between the purely O and the purely CO_2 atmosphere.

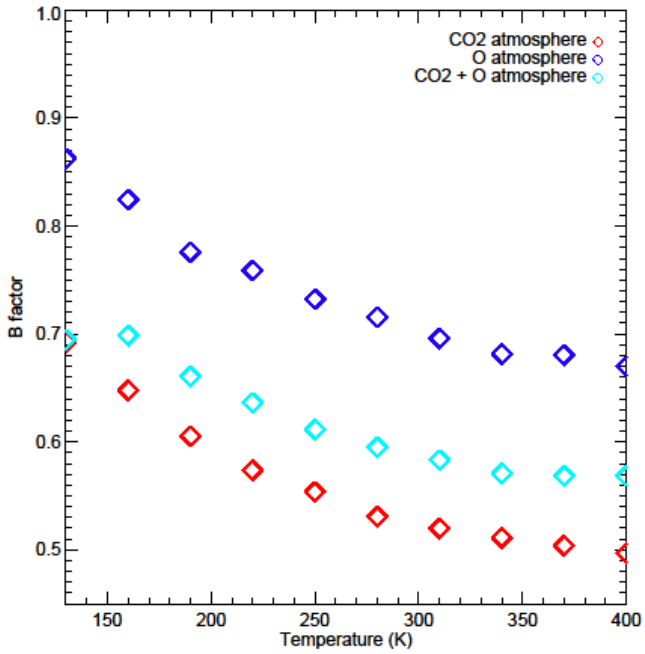

Fig. 5 Simulated B factor for Mars with the spherical model for different thermospheric temperature, and three different compositions of the Martian thermosphere (100% CO_2 in red), (100% O in dark blue) and (1% O ; 99% CO_2 at 140 km in light blue.

This result confirms that B should differ from a purely O atmosphere and a purely CO_2 atmosphere because the rate of repopulation of the tail of the velocity distribution is faster when the masses of the collisional particles are close (Chamberlain and Smith 1971). Considering different values of the cross sections, will change the position of the exobase and could modify B. However, assuming a cross section between $1x10^{-15}$ cm^2 and 10^{-14} cm^2 change B by less than 2%, so it could explain only partly the differences with the B factor derived by Pierrard (2003).

4.3) Non-uniform temperature profile

In this section, the effect of a non-uniform temperature profile is studied, using a background atmospheric temperature profile similar to Terada et al. (2016) and a cross section of 10^{-14} cm^2. A

comparison of the simulated upward velocity and hydrogen kinetic temperature profiles for two different atmospheric temperature profiles is shown in Fig. 6. The results are in reasonable agreement, showing similar trends: a decrease of the kinetic temperatures above the exobase, and an increase of the upward velocity with a change in the slope near the exobase. As expected at low altitude the hydrogen kinetic temperature is equal to the atmospheric temperature due to the collisions. The magnitude of the upward velocity is also in agreement with Terada et al. (2016) with upward velocity ~ 2-3 m/s for the simulation with an exospheric temperature of 210 K and upward velocity ~ 10 – 40 m/s for the simulation with a temperature of 360K. For the first case, the simulated hydrogen kinetic temperature at 250 km differs by less than 5% compared to Terada et al. (2016), while the difference for the second case at 400 km, the difference is of 10%. The difference for the upward velocity is 20% for the first case and 40% for the second case at 250 and 400 km respectively.

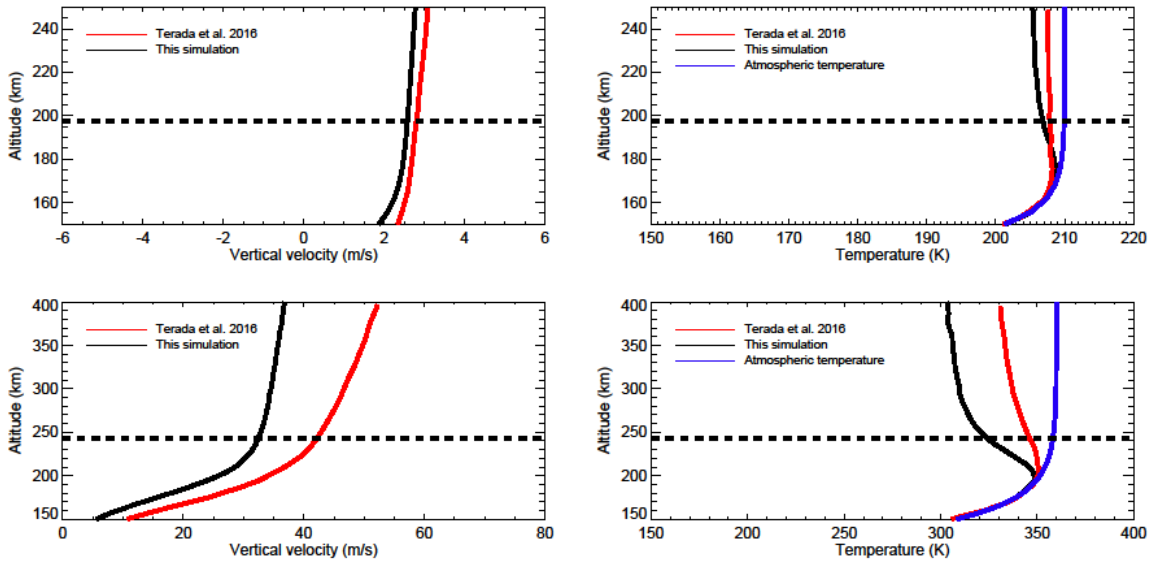

Fig. 6 : Simulated hydrogen vertical velocity (left column) and kinetic temperature (right column) for two atmospheric temperature profiles from Terada et al. (2016) : 210K (top panels) and 360 K (bottom panels). The simulated profiles by Terada et al. (2016) are also shown for comparison. The horizontal black dashed line indicates the altitude of the exobase for the two simulations.

413 The collisions between hot oxygen and hydrogen atoms, included in the simulations of Terada et
414 al. (2016) but not in our simulations, could heat the hydrogen and increase its escape flux and then
415 the upward velocity. For these two simulations, the simulated values of B are 0.58 and 0.50
416 respectively. These values are slightly lower (~ 3%) than those simulated with an isothermal
417 atmosphere at 210 and 360 K (0.59 and 0.51 respectively). For the non-isothermal simulations, a
418 part of the escaping particles come from below the exobase, where the temperature is lower than
419 the exospheric temperature. Then, the escape is slightly less efficient and B is reduced. However,
420 the difference is small and an isothermal profile is a reasonable assumption to estimate B on Mars

421

422 **5) Pluto simulations**

423 On Pluto, the exospheric temperature has been derived during the New-Horizons flyby from the
424 density vertical profile of N_2 (the dominant species below the exobase) and CH_4 obtained by stellar
425 occultations (Gladstone et al. 2017). The exospheric temperature was 68 K, lower than the model
426 predicted temperatures (100K) before the New-Horizons fly-by. The observations show that the
427 atmosphere of Pluto is not in slow hydrodynamics escape in contrast to the predictions of several
428 fluid models (Krasnopolsky 1999, Strobel et al. 2008). However, even before the fly-by of New-
429 Horizons, the slow hydrodynamics escape model has been shown to be invalid by several kinetic
430 models (Volkov et al. 2011, Tucker et al. 2012, Erwin et al. 2013).

431 Because of the large eccentricity of the Pluto's orbit, the exospheric temperature could be highly
432 variable. In our model, we consider exospheric temperatures from 40 to 100 K. The atmosphere is
433 mainly composed of N_2 and in all the simulations, we consider a N_2 density of 10^{10} cm^{-3} at 650 km
434 (Krasnopolsky 2020), an isothermal and barotropic atmosphere and assume that most of the

435 hydrogen atoms are produced below 650 km. The upper limit is at 5650 km, and the spatial
436 resolution is 20 km. For T = 100K, the escape parameter of N_2 at the exobase becomes low ~ 11
437 and the density profile could slightly differ from the hydrostatic profile due to the outflow of the
438 atmosphere (e.g. Volkov et al. 2011). A full DSMC (e.g. Tucker et al. 2013) would be needed to
439 extend our results to lower values of the escape parameter.

440 The chosen range of temperature at the exobase corresponds to escape parameters λ for atomic
441 hydrogen at the exobase varying from 0.4 to 0.9. B variations vs. Exospheric temperature for atomic
442 hydrogen are displayed on Fig. 7. At such low λ values, B increases with the temperature, so even
443 if the escape parameter is very low, the Jeans flux at the exobase is a better estimate of the real
444 thermal escape on Pluto than Mars and Earth. Contrary to Mars and Earth simulations, the slope of
445 the two models is different, suggesting the assumptions of the plane parallel start to break down
446 for higher temperature. But even if the assumptions of a hydrostatic background atmosphere used
447 for the spherical model become questionable and only a full DSMC model become valid.

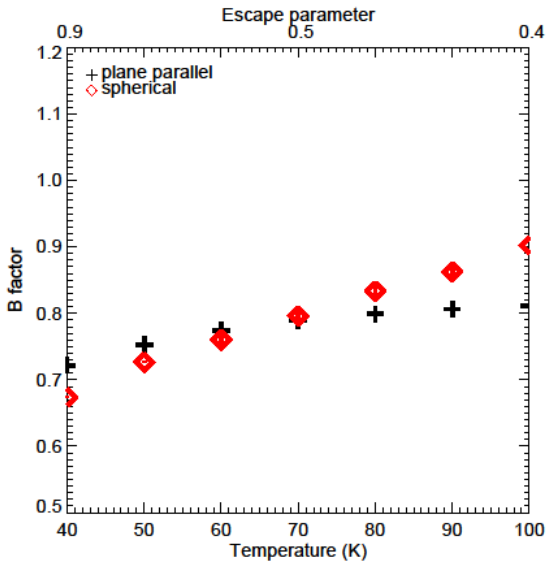

448

449 *Fig. 7: Simulated B factor for Pluto for the slab isothermal model (black) and the spherical isothermal model (red) at*
450 *different atmospheric temperatures.*

In this range of escape parameter, most of the atoms reaching the exobase have a velocity larger than the escape velocity and therefore most of the hydrogen atoms reaching the exobase should escape on Pluto. Therefore, when T increases (λ decreases), the velocity filtering of the atoms at the exobase becomes weaker and the velocity distribution, for upward-directed particles, at the exobase is closer to a Maxwellian velocity distribution (Fig. 8). The downward directed particles at the exobase are produced by the few collisions occurring above the exobase. Since a larger fraction of the particles reaching the exobase escape when λ decreases, the depletion in downward directed particles increases (Fig. 9). These two effects lead to an increase of A (see appendix) (Fig. 10) and B.

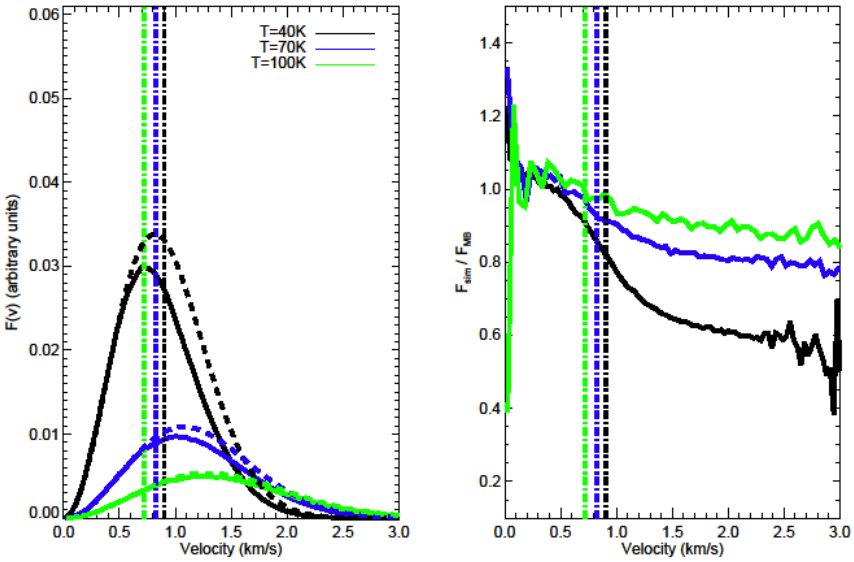

Fig. 8 Left: Simulated velocity distribution function at the exobase averaged over the upward-directed directions for three different exospheric temperatures with the spherical model (solid lines). The untruncated Maxwell-Boltzmann velocity distribution function at the exospheric temperature are also displayed (dashed lines). The three vertical dashed lines indicate the value of the escape velocity at the exobase. Right: Ratio of the simulated velocity distribution functions and the Maxwell Boltzmann velocity distribution function.

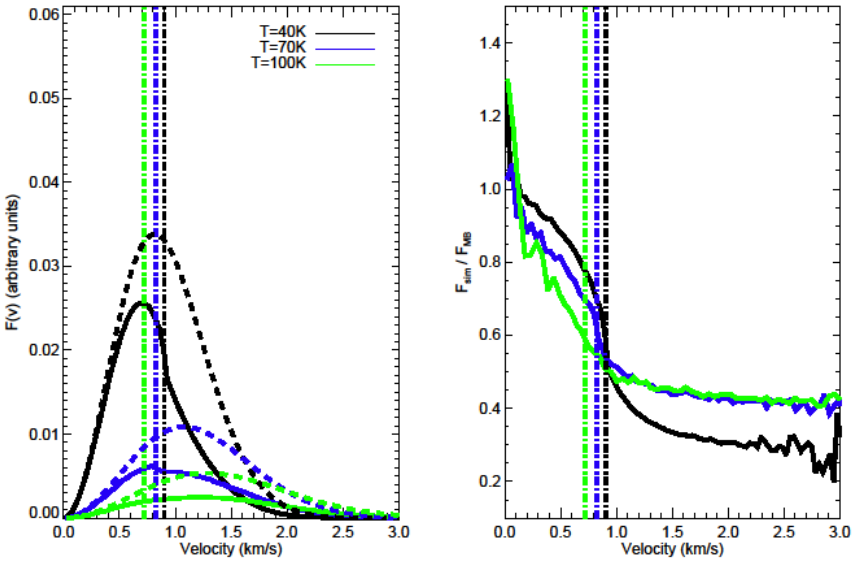

467

468 *Fig. 9 Left: Same as 8 but for the downward-directed particles.*

469 The decomposition in A and G factors is displayed on Fig. 9. As explained, A increases with T,

470 while the G factor remains almost constant, near 0.65, in this range of temperatures.

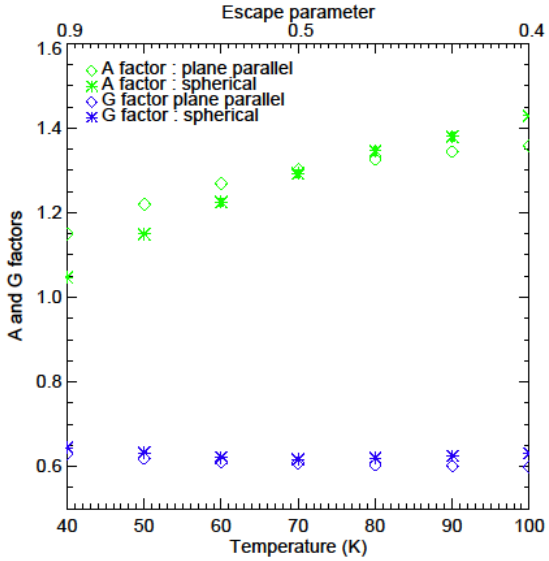

471

472 *Fig. 10: Simulated A and G factor for Pluto for the slab isothermal model (diamonds) and the spherical isothermal*
473 *model (stars) at different atmospheric temperatures.*

For the plane parallel simulations, the values of the three parameters B, A and G are very close to the asymptotic values obtained for Earth conditions (see section 3.2).

Due to the large effusion velocity at the exobase, the hydrogen density scale height is very far from the expected hydrostatic scale height. This is a direct consequence of Fick's law which dominates the gravity in the atomic diffusion. The efficiency of the escape (the low value of the escape parameter) quickly empties the thermosphere in hydrogen, which is slowly replenished from the lower atmosphere and therefore the escape rate is limited by this slow supply by diffusion. In order words, to maintain the vertical flux constant between the lower atmosphere (where the velocity is small) and the exobase (where the velocity is close to the effusion velocity) a large vertical variation of the density is needed. The variations of the hydrogen density from 650 km to 5650 km are shown in Fig. 10 for three different values of the temperature (40K, 70K and 100K), showing the strong effect of the escape rate on the hydrogen density profile and the scale height below the exobase.

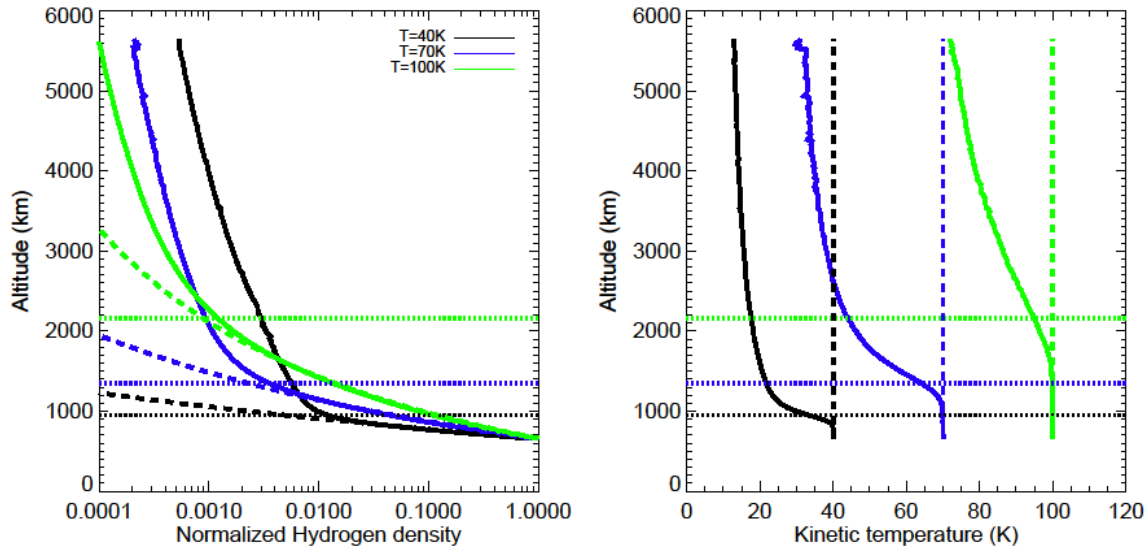

Fig. 11: Left Simulated hydrogen density profile at Pluto, normalized to 1 at the lower boundary for three different values of the exospheric temperature. The horizontal dotted lines indicate the altitude of the exobase for each model. The normalized atmospheric (N_2) density is shown by the dashed lines. Right : Simulated hydrogen kinetic temperature (solid lines), and atmospheric temperature (dashed lines).

When T increases, the global expansion of the N_2 atmosphere shifts upward the exobase altitude from ~ 1100 km at T = 40 to 2200 km at T = 100 K. Below the exobase, the hydrogen scale height is close to the atmospheric density scale height, while above the exobase it is close to the diffusion equilibrium scale height, as expected from the solution of the molecular diffusion equation when the flux is limited by diffusion (Hunten 1973). A similar limit was found by Tucker et al. (2013) for H_2 on Titan from DSMC simulations. As noted by Chamberlain and Campbell (1967), at high temperatures (low escape parameters), due to the sharp gradient of the hydrogen density near the exobase, the derived values of B, proportional to n_0/n_c, are very sensitive to the definition of the exobase altitude. For example, if we define Kn by $Kn(z)=(2^{1/2}N_a(z)\sigma)^{-1}$ instead of $(N_a(z)\sigma)^{-1}$ (see section 2), the altitude of the exobase increases and n_c/n_0 decreases. In that case the value of B is ~ 0.94 for T =70K. However, the variations of B, A and G with the temperatures, in the studied range with the escape parameters are not modified.

The simulated kinetic temperature is also shown on Fig. 11, showing the cooling of the hydrogen compared to the atmosphere. This decrease of the kinetic temperature is due to the loss of escaping particle that reduces the width of the velocity distribution. Finally, the atmosphere of Pluto is not a purely N_2 atmosphere but contain a small fraction of CH_4 near the exobase. A simulation, including 5% of CH_4 near 650 km (Young et al. 2018) at T = 70K, leads to an increase of B by ~ 5% (B = 0.837±0.006) suggesting that the hydrogen thermal escape rate is closest to the Jeans escape rate at the atmospheric temperature on Pluto, than Mars or the Earth.

6) Conclusion

A Monte Carlo test particle have been used to study the departure of the thermal escape rate from the Jeans escape rate at Earth, Mars and Pluto for current exospheric temperatures. This departure can be quantified by the ratio B between the thermal escape and the Jeans escape rates. At Earth and Mars, simulated B values are in very good agreement with previous study (Chamberlain and Shizgal 1971, Shizgal and Blackmore 1986) for the same assumptions, but differ from the results of Pierrard (2003) which may be due to numerical effects. We also find a minimum of B with the exospheric temperature near $\lambda = 3$ due to the fact that when λ becomes too low, the fraction of escaping particles become less dependent on the velocity (most of the particles have a velocity larger than the escape velocity) and then the distribution of the upward-directed particles becomes more Maxwellian, while the downward directed distribution is strongly depleted. For current temperatures at Earth and Mars, the B factor decrease with T, from ~ 0.9 at T = 700 K to ~0.7 at T = 2000 K for Earth and from ~0.7 at T = 130K to ~0.5 for T = 400 K at Mars. For Pluto, it increases with the temperature from ~ 0.7 at T = 40 K to ~0.9 at T = 100K. A Maxwellian velocity distributions in the exosphere is generally assumed to interpret the hydrogen Lyman-α emissions observed by planetary missions. This assumption is not valid above the exobase, where the velocity distribution is depleted at high velocity for downward directed particles for Mars, Earth and Pluto and for upward directed particles for Mars and Earth and will be investigated in the future. The simple assumptions used in the plane parallel model to estimate B are valid for low escape parameters investigated in this paper ($\lambda > 0.4$). Only a full DSMC approach could be used to check where this model breaks down.

Appendix

In this appendix, we consider a Truncated Maxwellian-Boltzmann (TMB) velocity distribution and the associated untruncated Maxwellian-Boltzmann (MB) distribution at the exobase, simulated with the plane parallel model, as illustrated on Fig. A1 and Fig A2 corresponding to different values of the escape parameter at the exobase λ_c.

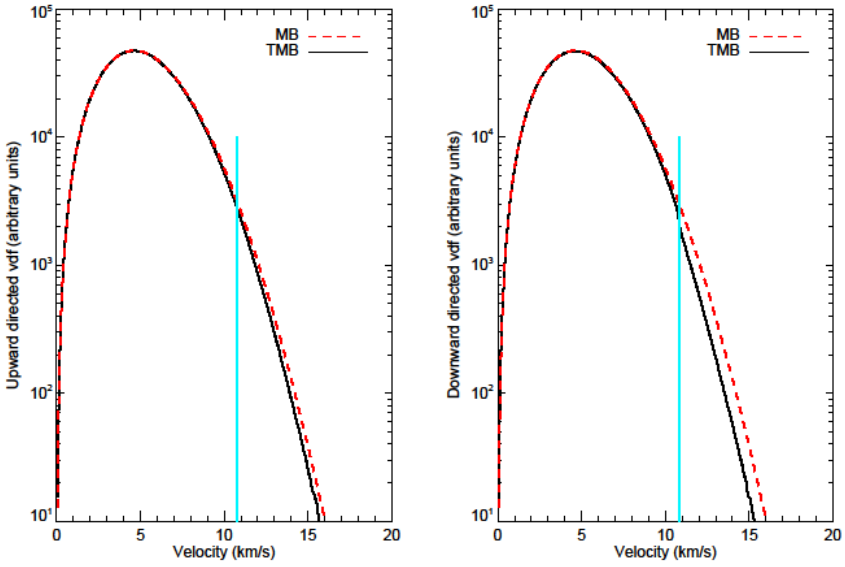

Fig. A1, Example of truncated Maxwellian-Boltzmann velocity distribution at the exobase for a large value of λc =5.4. Left: average distribution for the upward directed particles. Right: average distribution for the downward directed particles. The complete Maxwellian-Boltzmann distribution functions are also displayed in red. The escape velocity is indicated by the blue vertical line.

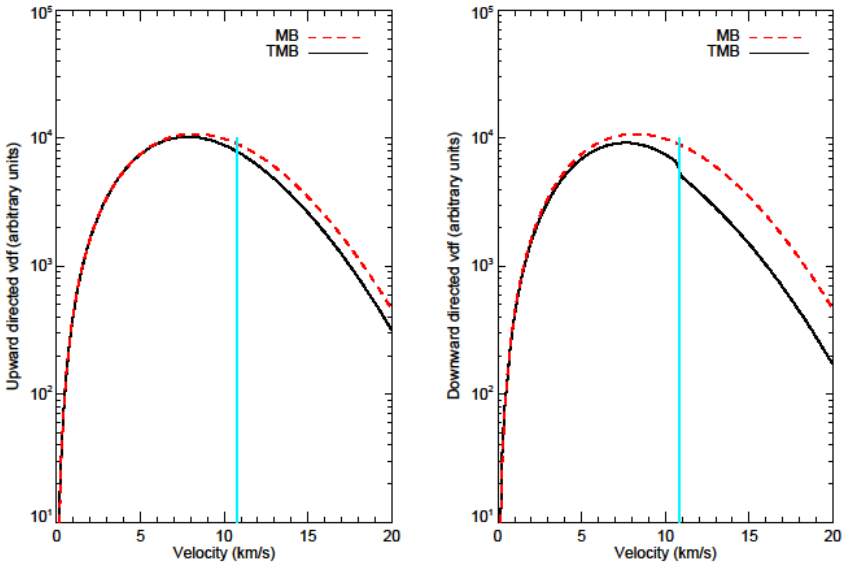

544

545 *Fig. A2, Example of truncated Maxwellian-Boltzmann velocity distribution at the exobase for a low value of λc =1.7.*
546 *Left: average distribution for the upward directed particles. Right: average distribution for the downward directed*
547 *particles. The complete Maxwellian-Boltzmann distribution functions are also displayed in red. The escape velocity is*
548 *indicated by the vertical line.*

549

550 The A factor (Eq. 12) is defined by

551 $$A = \frac{U_{eff}(TMB)}{U_{eff}(MB)} = \frac{F(TMB)}{F(MB)}\frac{n(MB)}{n(TMB)} = \frac{\left(1-\frac{(F(MB)-F(TMB)}{F(MB)}\right)}{\left(1-\frac{n(MB)-n(TMB)}{n(MB)}\right)} = \frac{1-\delta F/F}{1-\delta n/n}$$

552 For large values of λc (case 1), the decrease of the density δn/n is 2% while the decrease δF/F is
553 16% and therefore A ~ 1-δF/F = 0.84. For low values of λc (case 2), the large depletion of the
554 downward atoms strongly modifies the density but does not affect the escape flux. In that case, the
555 decrease of δn/n ~ 18.4% and the decrease δF/F 17.7%, so A is closer and even slightly larger than
556 1. A majorant value for A is 2 corresponding to a distribution fully depleted of downward directed
557 particles and untruncated of upward directed particles (i.e., δF/F = 0 and δn/n = ½). The largest
558 simulated value in this study is ~1.4.

Acknowledgements,

This work has been supported by French INSU programs PNP and PNST. I thank F. Leblanc and two anonymous referees for their comments.

References

Baliukin, I. I., J-L. Bertaux, E. Quémerais, V.V. Izmodenov, and W. Schmidt, SWAN/SOHO Lyman-α mapping: The hydrogen geocorona extends well beyond the Moon, J. Geophys. Res. Space Physics, 124, 861-885, (2019)

Beth, A., P. Garnier, D. Toublanc, I. Dandouras, C. Mazelle, and A. Kotova, Modeling the satellite particle population in the planetary exospheres: Application to Earth, Titan and Mars, Icarus, 227, 21-36, (2014)

Bird, G.A., Molecular Gas Dynamics and the Direct Simulation of Gas Flows. Clarendon Press Oxford, New York, (1994)

581 Bougher, S.W. et al., Early MAVEN deep dip campaigns: first results and implications, Science,
582 350, doi: 10.1126/science.aad0459, (2015)

583 Bougher, S.W., et al., The structure and variability of the Martian dayside thermosphere from
584 MAVEN/NGIMS and IUVS measurements: Seasonal and solar activity trends in scale
585 heights and temperatures, J. Geophys. Res. Space Physics, 122, 1296-1313, (2017)

586 Brinkmann, R.T., Departure from Jeans' escape rate for H and He in the Earth's atmosphere,
587 Planet. Space Sci., 18, 449-478, (1970)

588 Butler, B.J., The migration of volatiles on the surfaces of Mercury and the Moon, J. Geophys.
589 Res., 102, 19,283-19,291, (1997)

590 Chamberlain, J.W., Planetary coronae and atmospheric evaporation, Planet. Space Sci., 11, 901-
591 960, (1963)

592 Chamberlain, J.W., and F.J. Campbell, rate of evaporation of a non-maxwellian atmosphere,
593 Astrophys. J., 149, 687- 705, (1967)

594 Chamberlain, J. W., and G.R. Smith, Comments on the rate of evaporation of a non-maxwellian
595 atmosphere, Planet. Space Sci., 19, 675-684, (1971)

596 Chapman, S., and T.G. Cowling, The mathematical theory of non-uniform gases, Cambridge
597 University Press, New York, (1970).

598 Chassefière, E. and F. Leblanc, Mars atmospheric and evolution; interaction with the solar wind,
599 Planet. Space Sci., 52, 1039-1058, (2004)

600 Dickinson, R.E., E.C. Ridley, and R.G. Roble, Thermopsheric general circulation with coupled
601 dynamics and composition, J. Atm. Sci., 41, 205-219 (1984)

602 Erwin, J., O. J. Tucker, and R. E. Johnson, Hybrid Fluid/Kinetic Modeling of Pluto's Escaping
603 Atmosphere., Icarus 226(1), (2013)

604 Fox, J. The chemistry of protonated species in the Martian ionosphere, Icarus, 252, 356-392,
605 (2015)

606 Gladstone, G.R. et al., The atmosphere of Pluto as observed by New Horizons, Science, 351,
607 10.1126/science.aad8866, (2016)

608 Gladstone, G.R., J.A. Krammer, Y.L. Yung, W.R. Pryor, and S.A. Stern, Constraining Pluto's H
609 and CH4 profiles with Alice Lyman-alpha observations, Pluto System After New
610 Horizons, held 14-18 July, 2019 in Laurel, Maryland. LPI Contribution No. 2133, 2019,
611 id.7071, (2019)

612 Gonzalez-Galindo, F., M.A. Lopez-Valverde, F. Forget, M. Garcia-Comas, E. Millour, and L.
613 Montabone, Variability of the Martian thermosphere during eight Martian years as
614 simulated by a ground-to-exosphere model global circulation model, J. Geophys. Res.
615 Planets., 120, 2020-2035, (2015)

616 Huebner, W.F., Solar photo rates for planetary atmospheres and atmospheric pollutants,
617 Astrophys. Space Sci., 195, 1-294, (1992)

618 Hunten, D.M., The escape of H_2 from Titan, J. Atm. Science, 30, 726-732

619 Krasnopolsky, V.A., Hydrodynamic flow of N2 from Pluto, J. Geophys. Res., 104, 5955-5962,
620 (1999)

621 Krasnopolsky, V.A., Mars' upper atmosphere and ionosphere at low, medium, and high solar
622 activities: Implication for evolution of water, J. Geophys. Res., 107, E12, 5128,
623 doi:10.1029/2001JE001809, (2002)

624 Krasnopolsky, V.A., A photochemical model of Pluto's atmosphere and ionosphere, Icarus,
625 335,113374, (2020)

626 Leblanc, F., et al., On the origins of Mars' exospheric nonthermal oxygen component as observed
627 by MAVEN and modeled by HELIOSARES, J. Geophys. Res., Planets, 122, 2401-2428,
628 (2017)

629 Lewkow, N.R., and V.K. Kharchenko, Precipitation of energetic neutral atoms and induced non-
630 thermal escape fluxes from the Martian atmosphere, Astrophys. J., 790:98, (2014)

631 Pierrard, V., Evaporation of hydrogen and helium atoms from the atmosphere of Earth and Mars,
632 Planet. Space Sci., 51, 319-327, (2003)

633 Shizgal, B., and R. Blackmore, A collisional kinetic theory of a plane parallel evaporating
634 planetary atmosphere, Planet. Space Sci., 34, 279-291, (1986)

635 Strobel, D.F., N2 escape rates from Pluto's atmosphere, Icarus, 193, 612-619, (2008)

636 Terada, K., N. Terada, H. Shinagawa, H. Fujiwara, Y. Kasaba, S. Kanako, F. Leblanc, J-Y.
637 Chaufray, and R. Modolo, A full-particle Martian upper thermosphere-exosphere model
638 using the DSMC method, J. Geophys. Res: Planets, 121, 1429-1444, doi:
639 10.1002/2015JE004961, (2016)

640 Tucker, O. J., J. T. Erwin, J. I. Deighan, A. N. Volkov, and R. E. Johnson, Thermally Driven
641 Escape from Pluto's Atmosphere: A Combined Fluid/Kinetic Model., Icarus 217(1):408–
642 15, (2012)

643 Tucker, O.J., R.E. Johnson, J.I. Deighan, and A.N. Volkov, Diffusion and thermal escape of H2
644 from Titan's atmosphere: Monte Carlo simulations, Icarus, 222, 149-158, (2013)

645 Volkov, A.N., R.E. Johnson, O.J. Tucker, and J.T. Erwin, Thermally-driven atmospheric escape:
646 Transition from hydrodynamic to Jeans escape, Astrophys. J., 729, L24, 1-5, (2011)

647 Young, L.A., J.A. Kammer, A.J. Steffl, G.R. Gladstone, M.E. Summers, D.F. Strobel et al.,
648 Structure and composition of Pluto's atmosphere from the New Horizons solar ultraviolet
649 occultation, Icarus, 300, 174-199, (2018)